Journal of Materials Science & Technology 51 (2020) 32–39

Contents lists available at ScienceDirect

Journal of Materials Science & Technology

journal homepage: www.jmst.org

Research Article

Synthesis of yttrium iron garnet/bismuth quantum dot heterostructures with localized plasmon enhanced magneto-optical performance

Lichuan Jin[a,*], Caiyun Hong[b], Dainan Zhang[a], Peng Gao[c,d], Yiheng Rao[a], Gang Wang[a], Qinghui Yang[a], Zhiyong Zhong[a], Huaiwu Zhang[a,*]

[a] *State Key Laboratory of Electronic Thin Films and Integrated Devices, University of Electronic Science and Technology of China, Chengdu, 610054, China*
[b] *School of Science, Westlake University, Hangzhou, 310024, China*
[c] *Electron Microscopy Laboratory, and International Center for Quantum Materials, School of Physics, Peking University, Beijing, 100871, China*
[d] *Collaborative Innovation Centre of Quantum Matter, Beijing, 100871, China*

ARTICLE INFO

Article history:
Received 20 January 2020
Received in revised form 1 February 2020
Accepted 1 February 2020
Available online 31 March 2020

Keywords:
Electron energy loss spectroscopy
Surface plasmon resonance
Magneto-optical materials
Bismuth quantum dot
Ferromagnetic resonance

ABSTRACT

Interactions between light and magnetic matter attracted great attention lately due to their potential applications in nanophotonics, spintronics, and high-accuracy sensing. Here, we grew bismuth quantum dots (Bi–QDs) with strong spin–orbit coupling on a magnetic insulator yttrium iron garnet (YIG) via molecular beam epitaxy. The YIG/Bi–QDs material shows an enhanced magneto-optical Kerr rotation up to 130% compared with that of a bare YIG film. The Bi–QDs were also introduced onto a lutetium–bismuth co-doped YIG film to form a hybrid system with remarkably enhanced Kerr rotation (from 1626 to 2341 mdeg). Ferromagnetic resonance measurements showed an increased effective magnetization as well as interfacial spin–orbit field in the YIG/Bi–QD heterostructures. Localized plasmons were mapped using electron energy loss spectroscopy with high spatial resolution, revealing enhanced plasmon intensity at both the Bi–QD surface and YIG/Bi–QD interface. Introducing Bi-QDs onto the YIG film enhanced Kerr rotation owing to the attenuated optical reflection and increased effective magnetization. The Bi–QD-enhanced magneto-optical effect enables development of efficient nanoscale light switching, spintronics, and even plasmonic nano-antennas.

© 2020 Published by Elsevier Ltd on behalf of The editorial office of Journal of Materials Science & Technology.

1. Introduction

Light has both spin and orbital angular momentum, which determine many of its dynamic properties. Usually, the spin–orbit coupling (SOC) of photons is very weak, and observing SOC effects has typically relied on quantum weak measurements [1]. Enhanced light SOC has been explored in plasmonic metal nanostructures and could be harnessed for nanophotonic applications [2]. Interactions between light and condensed matter have received much attention because of potential applications in nanophotonic components and circuits [3–5]. Studies have shown that metal optical components can enhance typically weak magneto-optical (MO) effects [6–9]. Chin and co-workers demonstrated a plasmonic MO heterostructure with greatly enhanced Faraday rotation in a patterned periodic array of gold nanowires on a bismuth–iron garnet film [10]. Most studies of surface plasmons have focused on noble metals such as gold and silver. However, these metals must be combined with optically active materials to provide active control of plasmons. In particular, magneto-plasmons can be controlled with a magnetic field applied to a magnetic-metal hybrid system [11,12].

The magneto-optical Kerr effect (MOKE) converts linearly polarized light into elliptically polarized light in MO materials. Recently, the MOKE has been used to detect SOC-related torque in magnetic films, such as insulating yttrium–iron garnet (YIG) and metallic CoFeB, and heavy-metal Pt heterostructures via the interactions between electron spin angular momentum and light [13,14]. The MOKE in YIG is small for near-infrared wavelengths. Substituting yttrium with bismuth or a rare-earth element can enhance the MOKE with only small changes in the magnetic moment [15–18]. The large MO effect in Bi- or Ce-doped YIG stems from intra-atomic orbital dipole transitions between the 4f and 5d states of Ce or inter-

---

* Corresponding authors.
E-mail addresses: lichuanj@uestc.edu.cn (L. Jin), hwzhang@uestc.edu.cn (H. Zhang).

https://doi.org/10.1016/j.jmst.2020.03.025
1005-0302/© 2020 Published by Elsevier Ltd on behalf of The editorial office of Journal of Materials Science & Technology.

atomic dipole transitions between the 4f states of Ce and 3d states of Fe [19]. In fact, Bi is an interesting semimetal with strong SOC [20]. Two-dimensional Bi has been theoretically predicted to have a quantum spin Hall effect and enhanced magnetic response [21,22]. Tse and MacDonald predicted a large MOKE in the Bi_2Se_3 thin film owing to a delicate interplay between the thin-film cavity confinement and surface Hall conductivity of helical quasiparticles [23]. Moreover, Bi nanostructures show exceptional plasmonic properties in the visible-ultraviolet and far-infrared regions [24]. Thus, further investigations of MO properties in nano-sized Bi/magnetic-insulating heterostructures are important for developing advanced nanophotonic devices and circuits.

Here, we grew Bi quantum dots (Bi–QDs) using molecular beam epitaxy (MBE) on a single-crystalline YIG film, yielding a strongly enhanced MOKE in the YIG/Bi–QD hybrid system. The enhanced MOKE results from the attenuated optical reflection and increased effective magnetization in Bi–QDs. Localized plasmons were mapped using electron energy loss (EEL) spectroscopy with high spatial resolution, revealing greatly enhanced plasmon resonance at both the Bi–QD surface and YIG/Bi–QD interface. Ferromagnetic resonance measurements showed an increased effective magnetization and interfacial spin–orbit field in the YIG/Bi–QD system. The Bi–QD-enhanced MOKE we discovered offers greater ability to develop 2D magneto-optical materials.

2. Experiments and methods

2.1. Material preparations

The magnetic layer was a 400-nm-thick single-crystal YIG film with the composition $La_{0.03}Y_{2.97}Fe_5O_{12}$, grown via liquid-phase epitaxy on gadolinium–gallium garnet $Gd_3Ga_5O_{12}$ (GGG) substrates at 970 °C. Lanthanum was substituted for better lattice matching. After cleaning with acetone, alcohol, and a mixture of H_2SO_4 and H_2O_2, the single-crystalline YIG film was annealed at 500 °C for 2 h in an MBE chamber to restructure the YIG surface. The Bi–QDs then self-assembled on the YIG film at 200 °C with a pressure of 5×10^{-10} Torr and growth rate of 0.003 nm/s. The Bi–QDs have large surface area and they are easy to react with the oxygen in air. So, all the samples should be kept in vacuum chamber to avoid the oxidation.

2.2. Material characterizations

To measure ferromagnetic properties, we used a vector network analyzer ferromagnetic resonance (VNA-FMR) spectrometer to determine the change in magnetic properties of the YIG/Bi–QD heterostructure. The coplanar waveguide was 50 Ω impedance-matched and could transmit microwave frequencies up to 40 GHz. The vector network analyzer then applied a −10 dBm power to the micro-strip line and recorded the complex transmission parameter S at a fixed frequency with a sweeping magnetic field. The polar MOKE was measured with a Kerr magnetometer (Nano-MOKE3, British Durham Corp.) with a polarization sensitivity of 0.5 mdeg. The laser spot could be focused to a size as small as 2 μm at a wavelength of 660 nm. Raman spectra were measured with a confocal Raman microscope (InVia, Renishaw, UK). The laser spot was focused to 1 μm at 514 nm. We performed the photoluminescence measurements using a spectrophotometer (Model F-7000 FL, Hitachi) with a 220 nm xenon lamp to detect the fluorescence spectrum. Atomically resolved microstructures were characterized with a spherical aberration-corrected scanning transmission electron microscope (AC–STEM; Titan Cubed Themis G2 300) operated at 300 kV. Elemental maps of the YIG/Bi–QDs were collected in STEM mode with energy dispersive X-ray (EDX) detectors. High-spatial-resolution EEL spectroscopy was performed in STEM mode to characterize the localized surface plasmons in the YIG/Bi–QD hybrid system with an incident electron beam energy of 60 keV.

Table 1
Size and distribution of different samples as determined by atomic force microscopy and STEM. Each number in parentheses denotes the Bi–QD growth time (time, min).

Sample	Number per μm^2	Mean height (nm)	Mean diameter (nm)
YIG/Bi-QD(10)	4.9 ± 0.1	18.1 ± 0.1	29.8 ± 0.1
YIG/Bi-QD(20)	6.6 ± 0.1	31.9.±0.1	36.2 ± 0.1
YIG/Bi-QD(30)	12.7 ± 0.1	43.2 ± 0.1	55.1 ± 0.1
YIG/Bi-QD(40)	25.8 ± 0.1	45.8 ± 0.1	57.7 ± 0.1
YIG/Bi-QD(50)	38.5 ± 0.1	47.9 ± 0.1	60.4 ± 0.1

3. Results and discussion

3.1. Synthesis and surface morphology characterization

We examined the surface morphologies of the Bi–QDs using STEM. Figs. 1(a) and S1 (supplementary information) show noticeable nanoparticle morphology. Evidently, the Bi grows by island formation at the temperature of 200 °C. It appears that growth at an elevated temperature allows sufficient movement of the Bi atoms on the YIG film surface to assemble into nano islands, which do not coalesce to form thin films. As the growth time increased from 10 to 50 min, the Bi–QDs grew bigger and were more intensively distributed. After 30 min, their size had changed little (see Table 1). The STEM images in Fig. 1(a)–(c) show that the Bi–QDs in the sample YIG/Bi–QD(30) had a mean diameter of 55 nm and a height of 43 nm. The spatial distributions of bismuth, iron, yttrium, and oxygen were determined via STEM combined with EDX spectroscopy, as shown in Fig. 1(d)–(g). The elemental maps in Fig. 1(d) show sharp interfaces between the Bi–QDs and YIG film, which formed without any bismuth diffusion.

3.2. Ferromagnetic resonance properties of the YIG/Bi–QD hybrid system

Fig. 2 shows the dynamic magnetic properties of the YIG/Bi–QD system revealed by the ferromagnetic resonance (FMR) measurements. In Fig. 2(a), the static magnetic field H was fixed in-plane along the y axis, and the dynamic magnetic field h_{rf} was along the x axis. An in-plane rotational stage was used to rotate the sample, which is equivalent to rotating H and h_{rf}. The symbol S21 denotes the microwave transmission from port 1 to port 2. We performed angular-dependent FMR spectroscopy to determine the magnetic anisotropy field H_k. The FMR field H_{FMR} and azimuthal angle Φ_H have the cosine relationship [25,26]:

$$H_{FMR}=H_0-H_k\cos(2\Phi_H) \tag{1}$$

where H_0 is the in-plane resonance magnetic field without the magnetic anisotropy field H_k. As shown in Fig. 2(c), H_k changed slightly among the specimens irrespective of the crystal orientation of YIG. The average H_k values of YIG (100) and YIG (111) were 113.7 and 1.9 Oe, respectively, indicating that the Bi–QDs did not affect the magnetic anisotropy of the YIG/Bi–QD system. We measured the transmission parameter S_{21} as function of frequency to determine the effective magnetization $4\pi M_{eff}$ and effective damping parameter α_{eff}. The applied magnetic field H was fixed along the y axis in the xy plane.

At a fixed frequency of 11 GHz, the FMR field shifted downfield for longer Bi–QD growth times. The YIG/Bi–QD hybrid system had stronger microwave absorption than that of bare YIG, shown in Fig. 2(b). The FMR linewidth broadening ΔH is shown in Fig.

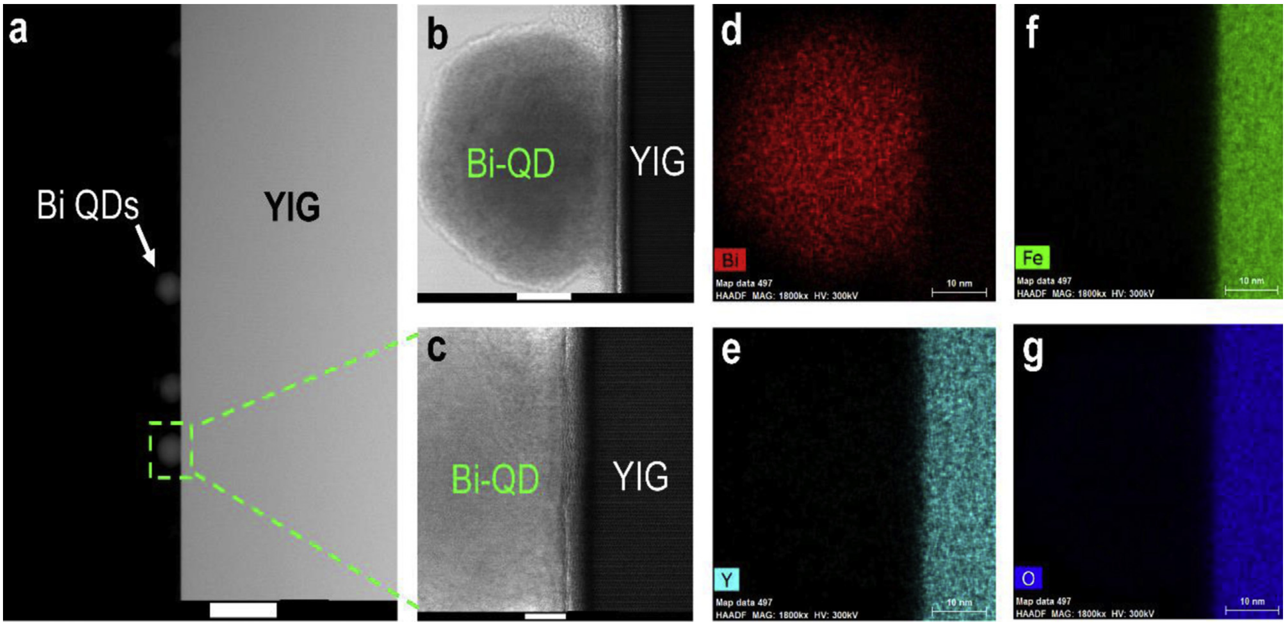

Fig. 1. (a) STEM image of Bi–QDs grown on a YIG film surface; the scale bar is 100 nm. (b) Bright-field (BF) image of a single self-assembled Bi–QD on a YIG film; the scale bar is 10 nm. (c) Expanded view of the BF image indicated by the square in (a); the scale bar is 5 nm. (d–g) EDX elemental mapping of bismuth, yttrium, iron, and oxygen, respectively; each scale bar is 10 nm.

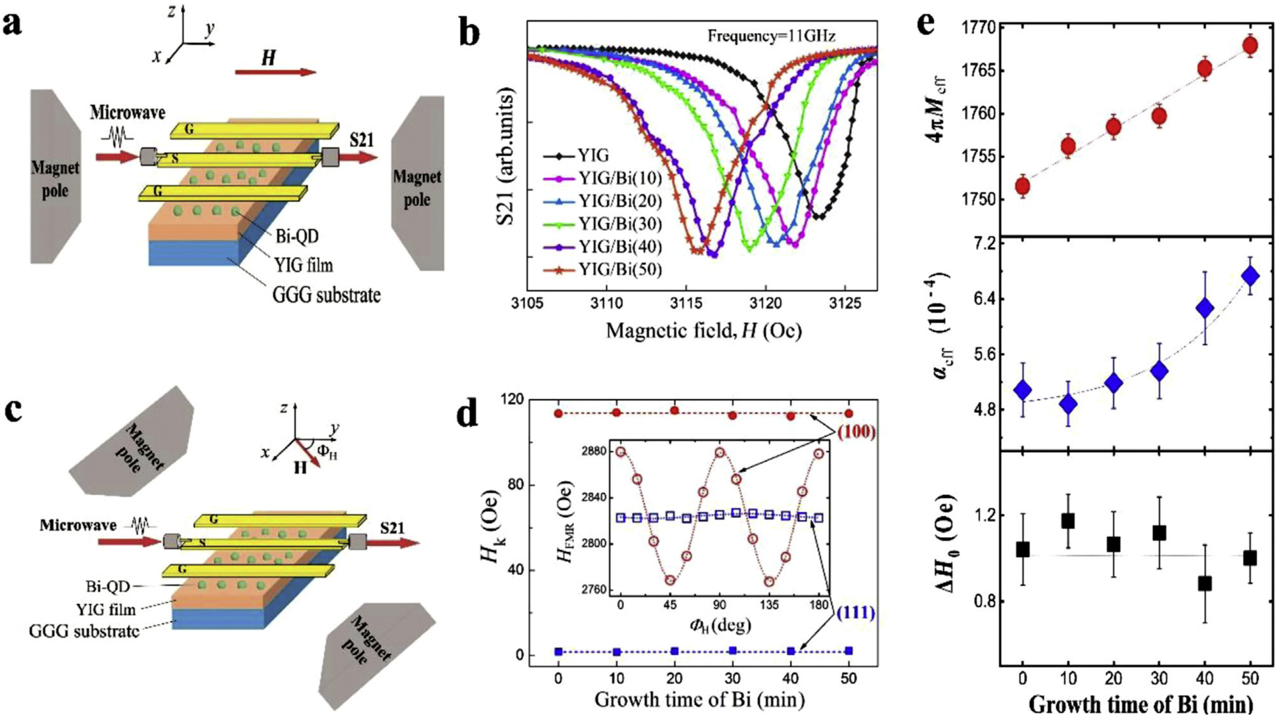

Fig. 2. (a) Schematic of the ferromagnetic resonance measurement. (b) H dependence of S_{21} in the YIG/Bi–QD specimen; the excitation frequency is 11 GHz, and the crystal orientation of the YIG substrate is (111). (c) Schematic of the angular-dependent FMR measurement. (d) Bi–QD growth-time dependence of the magnetic anisotropy field H_k for the crystal orientations (100) and (111) in YIG/Bi–QDs (marked by red dots and blue squares, respectively); the inset shows the resonance field H_FMR as a function of azimuthal angle Φ_H for YIG/Bi–QD (40) samples with substrates YIG (100) (red circles) and YIG (111) (blue squares). (e) Bi–QD growth-time dependence of the extracted inhomogeneous broadening ΔH_0 (black squares), effective damping parameter α_eff (blue diamonds), and effective magnetization $4\pi M_\mathrm{eff}$ (red dots) in YIG(111)/Bi–QDs.

S3 of the Supplementary Information. The effective magnetization $4\pi M_\mathrm{eff}$ can be determined from the Kittel formula:

$$f_\mathrm{FMR} = \gamma\pi_0\sqrt{(H_\mathrm{FMR}+H_\mathrm{k})+(H_\mathrm{FMR}+H_\mathrm{k}+4\pi M_\mathrm{eff})} \quad (2)$$

Where γ=2.8 MHz/Oe, and $\mu_0 = 4\pi\times10^{-7}$ H/m is the vacuum permeability. The value of $4\pi M_\mathrm{eff}$ increased linearly as the Bi–QD growth time increased, as shown in Fig. 2(e). The effective magnetization can be written as $4\pi M_\mathrm{eff} = 4\pi M_\mathrm{s}+H_\mathrm{SOF}+4\pi M_\mathrm{Bi\text{-}QD}$, where $4\pi M_\mathrm{s}$ is the saturation magnetization of YIG without considering the Bi-doping effect, H_SOF is the interfacial spin–orbit field, and $4\pi M_\mathrm{Bi\text{-}QD}$ is the Bi–QD magnetization. The parameter H_SOF is due to the interfacial Dzyaloshinskii-Moriya interaction (DMI) [27,28], which appears in a ferromagnet (FM) in contact with a heavy metal (HM) possessing a strong SOC. Thus far, there is no literature on the

DMI in Bi-QD/FM heterostructures. However, spin–orbit effects and DMI exist in HM/FM heterostructures regardless of whether the HM (such as Pt, Ta, or Bi) is in the form of a thin film, patterned metamaterial, or even nanostructure (a few nm) [29–31]. Kotaka and co-workers have reported large out-of-plane spin states on the Fermi lines of Bi nano films, where the maximum out-of-plane spin component was approximately 40% of the magnitude of the total spin [32]. As previously reported, an H-decorated Bi bilayer becomes a valley-polarized quantum anomalous Hall (QAH) insulator with a large band gap of 0.18 eV at the Fermi energy, with a magnetic moment of 1.0 μB per unit cell [33,34]. A large band gap of 0.18 eV has been observed in our studies using Fourier transform infrared (FTIR) spectroscopy, as discussed below.

As shown in Fig. 2(e), the effective Gilbert damping parameter α_{eff} can be extracted by fitting the FMR linewidth ΔH as a function of the resonance frequency f_{FMR} (see Fig. S3) [35]:

$$\mu_0 \Delta H = \mu_0 \Delta H_0 + \frac{2\alpha_{\text{eff}}}{\gamma} f \tag{3}$$

where γ is the gyromagnetic ratio, and μ_0 $\mu_0 \Delta H_0$ is the inhomogeneous linewidth broadening associated with the disorder or fluctuations in the magnetic film. The dependence of α_{eff} and ΔH_0 on the Bi–QD growth times is reasonable because when the Bi–QDs grow, the effective Gilbert damping parameter α_{eff} increases through pumping of the spin current into the adjacent Bi–QDs via the spin–orbit interaction [36–38]. Moreover, there was no inhomogeneous linewidth broadening when Bi–QDs were introduced onto the YIG film surface, indicating that the microstructures of the YIG film were unchanged after the Bi–QD growth.

3.3. Raman spectra and Fourier transform infrared-reflection properties of the YIG/Bi–QD hybrid system

The Raman spectra of the YIG/Bi–QDs and GGG are shown in Fig. 3(a) and (b), respectively. The YIG vibration modes are below 300 cm^{-1} and labeled as translations (T) of Y^{3+} and $[FeO_4]^{5-}$. The peaks v_2 (E_g) and v_2 (A_{1g}) represent two internal modes of the FeO_4 group [39]. After growth at 970 °C, Y_2O_3 and Fe_2O_3 have reacted to form YIG [40,41]. The characteristic peak of Fe_2O_3 at 290 cm^{-1} shifts to 272 cm^{-1} and is labeled $L[FeO_4]^{5-}$. The most intense Raman modes at 355, 524, and 741 cm^{-1} correspond to the three A_{1g} modes of internal vibrations of GaO_4 and GaO_6 in the GGG substrate. The lower-frequency A_{1g} mode can be assigned mostly to octahedral rotation and partly to tetrahedral rotation. The intermediate A_{1g} mode might be related to tetrahedral and octahedral bending. Meanwhile, the highest-frequency A_{1g} mode corresponds to symmetric tetrahedral and octahedral antiphase stretching [42]. There is no shift or change in the full width at half maximum of the vibration modes in the YIG/Bi–QD hybrid structure compared with those of the bare YIG film. As shown in Fig. 3(c) and (d), introducing the Bi–QDs enhanced the intensity of the two A_{1g} modes in GGG. Most plasmonic research, specifically surface-enhanced Raman scattering (SERS), is carried out using nanostructures of the noble metals Au and Ag [43–45]. In fact, the plasmonic activity in Bi nanostructures have been experimentally studied at visible-ultraviolet and far-infrared wavelengths [46,47]. Two theoretical models are used to describe the SERS enhancement. One is charge transfer, the excitation transfer of electrons from the metal to the molecule and back to the metal. The other is electric field enhancement, which is considered the main cause. Laser excitation of plasmon resonances greatly amplifies the electromagnetic field nearby. Near-field amplification close to the Bi–QDs enhances the optical intensity at the spatial position of the GGG/YIG dielectric substrate. This increases the magnitude of the induced dipoles, thus enhancing absorption and scattering. Bi-QDs can enhance Raman intensities of the GGG/YIG diaelectric substrate, particularly when the Bi–QDs increase in both size and density.

The optical reflection spectra of the YIG/Bi–QD system were characterized using FTIR spectroscopy in the frequency range from 20 μm (62 meV) to 3 μm (0.41 eV). Fig. 4(a) shows that when the Bi–QDs are introduced, they capture incident photons, which decreases the optical reflection intensity. It should be mentioned that the absorption peaks around 8.4 and 10.5 μm are due to the YIG substrate, which already exists in the bare YIG sample [48]. Interestingly, several attenuated reflection peaks appear at photon energies of 0.36 ± 0.005 eV (3.42 μm), 0.35 ± 0.005 eV (3.5 μm), 0.20 ± 0.005 eV (6.05 μm), and 0.18 ± 0.005 eV (6.85 μm). The attenuated peaks probably result from the optical absorption of the large band gaps in Bi–QDs. As the heaviest atom with a strong SOC, Bi is an important ingredient for both 2D and 3D topological insulators that host conducting surface states inside bulk insulators. In bulk, Bi displays interesting behavior at the Fermi level: a very low density of states characterizes the semimetal, and a shallow gap separates two filled s and three filled p bands from three empty p bands, but hole pockets at the T points and electron pockets at the L points cross the Fermi level [49]. For Bi–QDs, surface states of metallic character become dominant. These surface state bands can be strongly affected by SOC. From the absorption peaks at 0.35 eV (3.5 μm), 0.20 eV (6.05 μm), and 0.18 eV (6.85 μm), we conclude the MBE-grown Bi–QDs possess various surface state bands [33,34,50]. The band gap of 0.35 eV indicates the existence of QAH states in Bi–QDs. Although it is hard to directly determine the crystalline textures of Bi–QDs, FTIR is an efficient way to study their electronic and structural properties. Previous studies have shown that the buckled Bi (111) bilayer has a band gap of 0.2 eV, which is more energetically stable than the flattened sample because of sp^2 hybridization [51]. A band gap of 0.18 eV gradually appears as the amount of Bi–QDs increases. This is a signature of a mixed Weyl semimetal hydrogenated Bi (111) bilayer, which has out-of-plane magnetization [33].

The Bi–QDs over the surface of the YIG film emitted fluorescence under laser excitations at room temperature, as shown in Fig. 4(b). We attribute the enhanced fluorescence to the excitation of surface plasmon resonance (SPR) in the Bi–QDs [52,53]. Similarly to Au and Ag, Bi has been found to have plasmonic properties from the far-infrared to the ultraviolet region [54,55]. Collective excitations of free electrons in Bi–QDs give rise to SPR, which enhances optical absorption. This large SPR-mediated effect with Bi has been exploited in many applications, including sensors, fluorescence materials, and surface-enhanced spectroscopy [56].

3.4. Localized plasmon mapping of the YIG/Bi–QD hybrid system

The localized surface plasmons in YIG/Bi–QDs were experimentally observed using EEL spectroscopy at high spatial and energy resolution. As shown in Fig. 5(a), Bi–QDs were randomly distributed on the YIG surface. To obtain the EEL spectrum of a single Bi–QD, a focused electron beam was transmitted from the vacuum into one Bi–QD with a diameter of ~30 nm. The route of the incident electron beam is marked by a yellow arrow in Fig. 5(b). Spatially distributed EEL spectra of the YIG/Bi–QD system were extracted with a highly refined scanning electron probe along the route shown in Fig. 5(b). We observed four loss peaks in the energy range 0–32 eV, as presented in Fig. 5(c). The feature at 20 eV was the largest peak, which we assigned to a bulk plasmon of the YIG layer (as shown in Fig. S4 of the Supporting Information). This loss shows position-dependent behavior (marked by a purple dashed line). A loss at 3–7 eV was observed at the Bi–QD surface, which suggests that it originated from excitation of the localized surface plasmons. Two other losses appeared at 10.4 and 29.2 eV, which were only present at the center of the Bi–QD. These losses might correspond to the interband

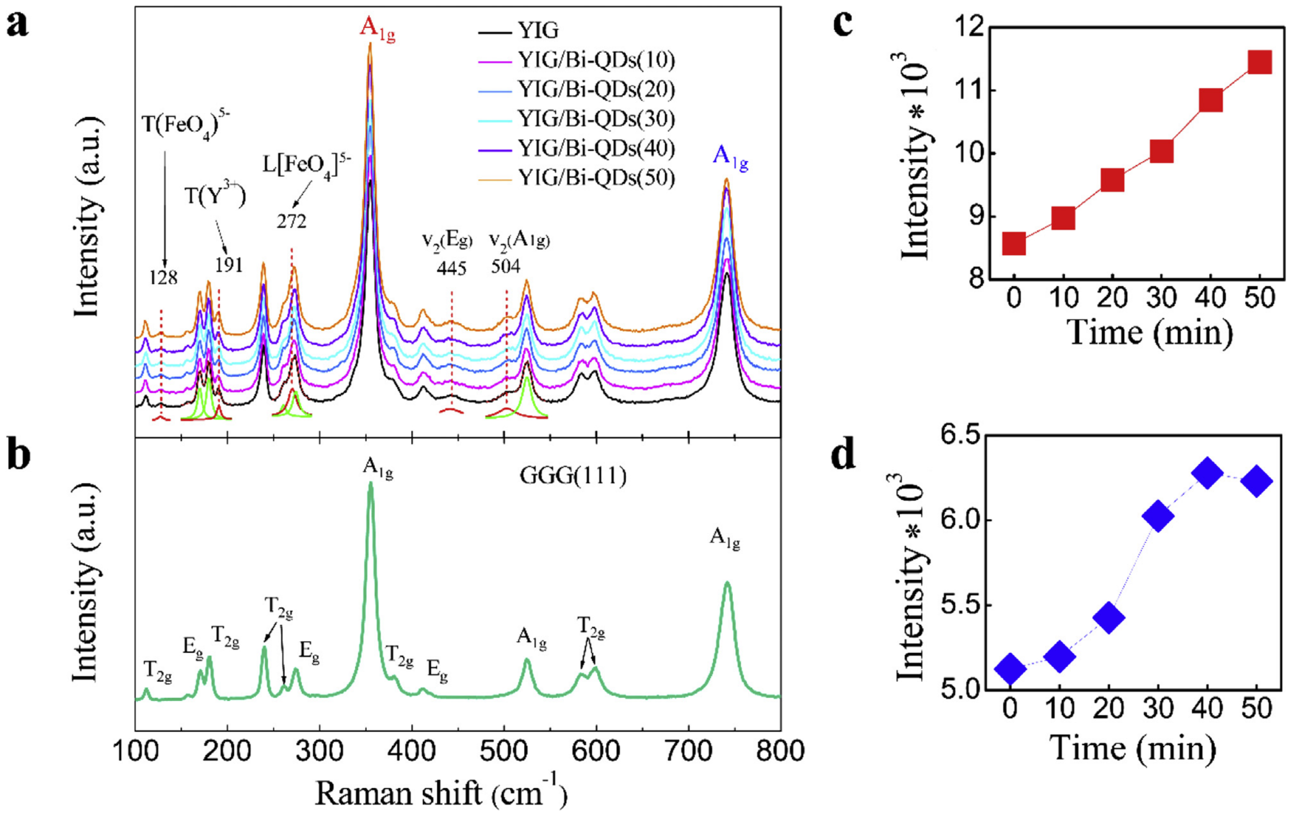

Fig. 3. (a) Raman spectra of the vibrational modes of the YIG/Bi–QD specimen; the red fitting lines show the YIG modes for a laser wavelength of 514 nm and laser power of 2 mW. (b) Raman spectra for the (111) orientation of the GGG substrate. Bi–QD growth-time dependence of the Raman intensity for two A_{1g} modes in GGG at (c) 355 cm^{-1} and (d) 741 cm^{-1}.

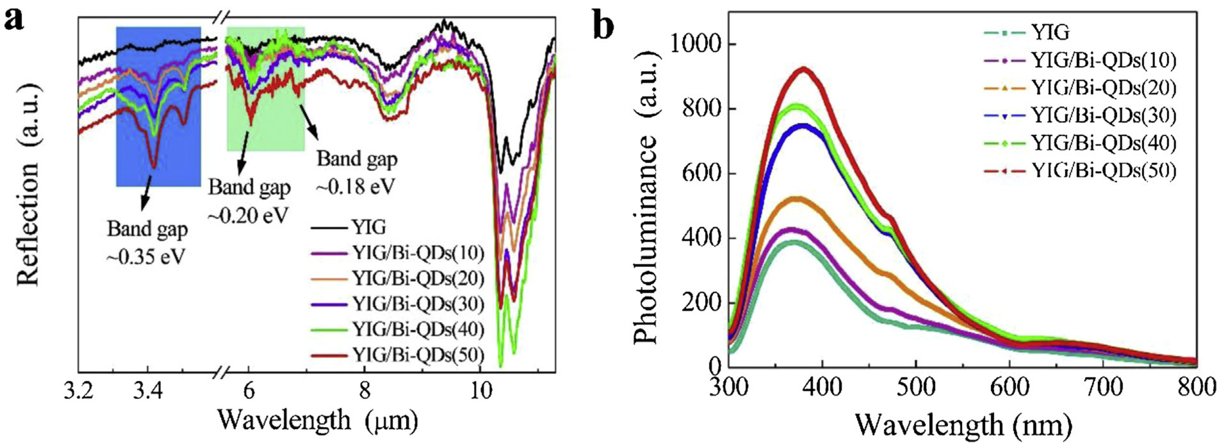

Fig. 4. (a) Fourier transform infrared spectroscopy of the YIG/Bi–QD system; the break in the spectra omits a featureless region. (b) Fluorescence spectra of the YIG/Bi–QD system obtained under 220 nm laser excitation; the inset shows Bi–QD growth-time dependence of the fluorescence peak in each sample.

transition of Bi 6 s and the transitions from the core Bi 5d level to the bottom of the conduction band, respectively [57]. We studied the position dependences of the plasmon intensity and energy, as shown in Fig. 5(d). Line intensity profiles were taken along the line X–X′ in Fig. 5(b) (the distance from the vacuum to the Bi–QD was ~7 nm, and the height of the single Bi–QD was ~25 nm). The plasmon energy and intensity were greatly enhanced at the Bi–QD surface and the YIG/Bi–QD interface. We obtained localized plasmon maps at different energy intervals (3–7, 16–23, and 28–32 eV) revealing enhanced plasmon intensity at both the Bi–QD surface and YIG/Bi–QD interface, as shown in Fig. 5(e)–(g). Notably, our results show that the localized surface plasmon was bent at the YIG/Bi–QD interface in the presence of a strong spin–orbit field, which indicates the existence of an interfacial magnetic field that affected both the spatial distribution and intensity of plasmons. The discovery gives the spin–orbit field a new role for producing plasmon excitations at the interfaces of magnetic films and heavy metals.

3.5. Magneto-optical Kerr properties of the YIG/Bi–QD hybrid system

The MOKE describes changes to light reflected from a magnetic surface and is associated with the off-diagonal components of the

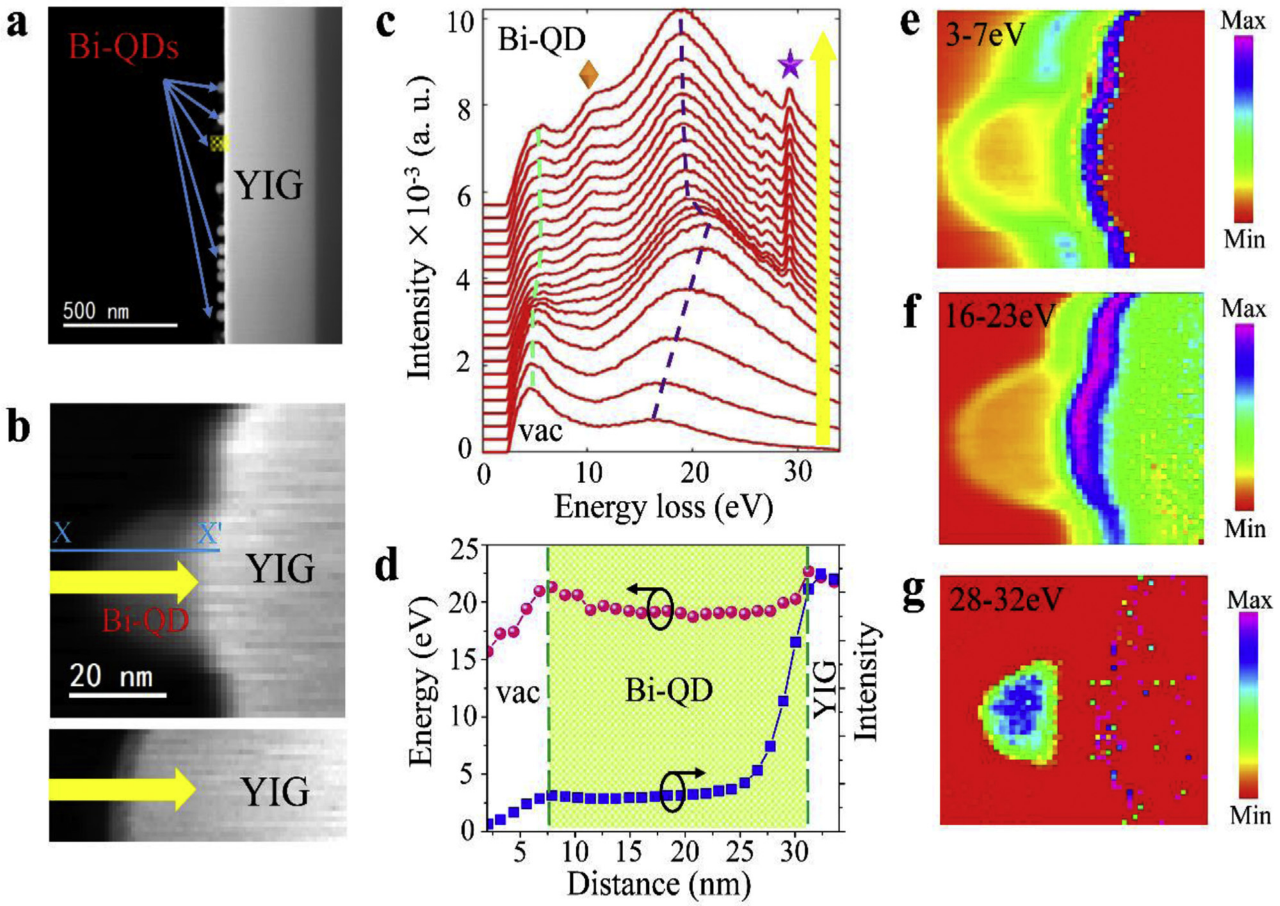

Fig. 5. Localized plasmon mapping. (a) Cross-sectional STEM image of the YIG/Bi–QD hybrid system. (b) High-angle annular dark-field image of an electron beam transmitted from the vacuum into a single Bi–QD and into the YIG film (the route of the incident electron beam is shown using a yellow arrow). (c) Spatially distributed EEL spectra of the YIG/Bi–QD system with an incident electron beam energy of 60 keV. (d) Position dependences of plasmon intensity and energy with line intensity profiles taken along the line X–X′ in (b); the distance from the vacuum to the Bi–QD is ~7 nm, and the height of a single Bi–QD is ~25 nm. EEL probability maps of the YIG/Bi–QD hybrid system corresponding to different electron energy intervals: (e) 3–7 eV; (f) 16–23 eV; (g) 28–32 eV.

dielectric tensor ε for the YIG/Bi–QD hybrid system. The external magnetic field and magnetizations were aligned perpendicular to the *xy* plane of the sample, corresponding to a polar MO Kerr configuration, as shown in Fig. 6(a). The dielectric tensor has the form as follows [58,59]:

$$\varepsilon = \begin{pmatrix} \varepsilon & a\prod_2 & 0 \\ a\prod_2 & \varepsilon & 0 \\ 0 & 0 & \varepsilon \end{pmatrix} \tag{4}$$

where ε is the (isotropic) diagonal tensor component, and $a\prod_2$ is the MO constant parameterizing the coupling strength between light and the out-of-plane magnetizations. The off-diagonal component $a\prod_2$depends on the applied perpendicular magnetic field, the magnetization of the YIG film, and the QAH state-induced magnetizations in Bi–QDs.

A large enhancement of the Kerr rotation was observed when the Bi–QDs were introduced, as shown in Fig. 6(b). Compared with the bare YIG film, the YIG/Bi–QD(50) hybrid system had a 130% enhancement of the MO Kerr signal. The MO activity of the YIG/Bi–QD system is the combined effect of the pure optical and MO properties of the whole heterostructure [58]. The complex Kerr rotation φ in our configuration is given by $\varphi = \theta_k + i\varphi = r_{ps}/r_{pp}$, where r_{ps} and r_{pp} are the pure MO and optical contributions. For the pure MO contribution, the Kerr rotation angle increased linearly with increasing effective magnetization $4\pi M_{eff}$ owing to the strong SOC-induced interfacial spin–orbit field and Bi–QD magnetizations [33,34]. The increased MO constant in the YIG/Bi–QD system demonstrated that the coupling between light and the out-of-plane magnetizations was indeed enhanced by the Bi–QDs. For the pure optical contribution, the incident light excites localized SPR in Bi–QDs, which can be considered an electric dipole. The electromagnetic amplification close to the Bi–QDs enhances the optical intensity at the spatial position of the YIG dielectric layer. This increases the magnitude of the induced dipoles, thus enhancing absorption and scattering, see the insert in Fig. 6(c). Only a small fraction of the photons escapes from the YIG/Bi–QD surface, resulting in decreased reflectivity. The effective photon capture in Bi–QDs attenuates reflection of the pure optical contribution r_{pp} according to the Kretschmann configuration [58]. In this instance, the decrease of this contribution directly affects enhancement of the Kerr rotation.

To confirm the mechanism of MOKE enhancement by the Bi–QDs, we substituted an MO garnet material, a lutetium–bismuth co-doped YIG (LBIG) film with a thickness of 3.5 μm, as the magnetic dielectric layer. The same series of Bi–QDs was grown on the LBIG film to form LBIG/Bi–QD hybrid structures. The polar Kerr rotations of the LBIG/Bi–QD systems were measured. Introducing the Bi–QDs into these heterostructures considerably enhanced the Kerr rotation from 1626 to 2341 mdeg, shown in Fig. 6(d). The results

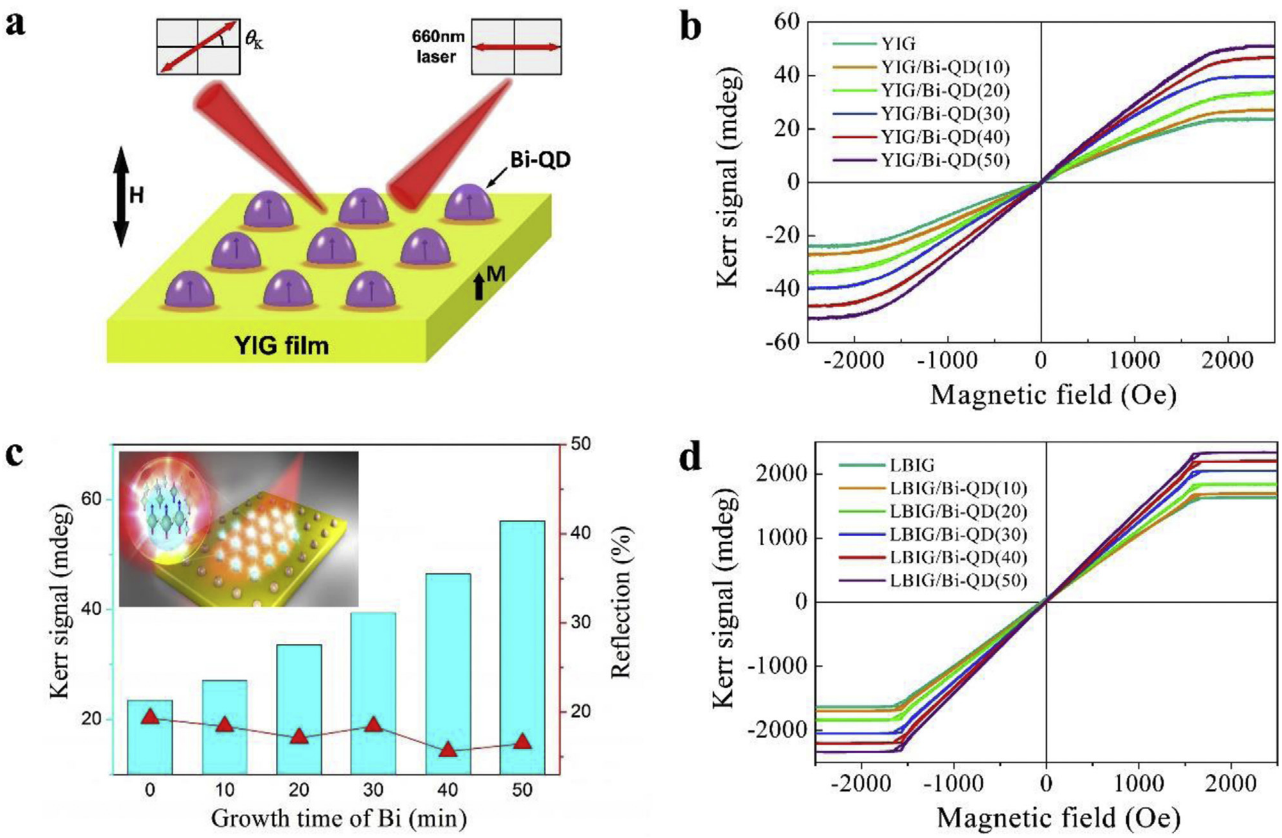

Fig. 6. (a) Schematic of the enhanced polar magneto-optical Kerr effect in a YIG/Bi–QD hybrid system. (b) Enhanced magneto-optical Kerr rotation was observed with the introduction of Bi–QDs. (c) Histogram of Bi growth-time dependence of the polar Kerr signal (red triangles mark reflections); the inset is a schematic of the enhanced magneto-optical Kerr effect in a YIG/Bi–QD hybrid system. (d) Polar magneto-optical Kerr rotation curves for a LBIG/Bi–QD hybrid system with varying Bi–QD growth time.

indicate that the Bi-QDs indeed significantly increase the Kerr rotation, revealing a new route to constructing high-performance MO devices using Bi–QDs.

4. Conclusion

In summary, we fabricated the first high-*Z* element Bi–QDs with diameters less than 60 nm on a magnetic insulating YIG film. This produced MO Kerr rotation up to 130% greater than that of bare YIG. VNA-FMR measurements showed an increased effective magnetization and interfacial spin–orbit field in the YIG/Bi–QD system. Highly resolved localized plasmon maps obtained via EEL spectroscopy revealed enhanced plasmon intensity at both the Bi–QD surface and YIG/Bi–QD interface. We attribute the large enhancement in MO Kerr rotation to attenuated optical reflection and increased effective magnetization by the Bi–QDs. This mechanism is unlike the MO mechanism in a Bi-doped YIG system. The Bi–QD-driven MOKE enhancement we discovered offers greater potential to develop 2D MO systems. This technique is versatile and can be adapted to studying the MO effect in any magnetic matter/Bi–QD configuration. It will have wide applications to nanoscale light switching, spintronics, and plasmonic nano-antennas.

Acknowledgments

This work was supported financially by the National Natural Science Foundation of China (Nos. 51702042, 61734002, 61571079 and 51672007) and the National Key Research and Development Plan (Nos. 2016YFA0300801 and 2016YFA0300804). The authors acknowledge Electron Microscopy Laboratory in Peking University for the use of Cs corrected electron microscope.

Appendix A. Supplementary data

Supplementary material related to this article can be found, in the online version, at doi:https://doi.org/10.1016/j.jmst.2020.03.025.

References

[1] O. Hosten, P. Kwiat, Science 319 (2008) 787–790.
[2] D. Pan, H. Wei, L. Gao, H. Xu,Phys. Rev. Lett. 117 (2016), 166803.
[3] H. Zhang, M. Kang, X. Zhang, W. Guo, C. Lv, Y. Li, W. Zhang, J. Han,Adv. Mater. 29 (2016), 1604252.
[4] Z. Li, Y. Li, T. Han, X. Wang, Y. Yu, B. Tay, Z. Liu, Z. Fang, ACS Nano 11 (2017) 1165–1171.
[5] L.W. Clark, L.C. Ha, C.Y. Xu, C. Chin,Phys. Rev. Lett. 115 (2015), 155301.
[6] M. Liu, X. Zhang, Nat. Photon. 7 (2013) 429–430.
[7] V.I. Belotelov, I.A. Akimov, M. Pohl, V.A. Kotov, S. Kasture, A.S. Vengurlekar, A.V. Gopal, D.R. Yakovlev, A.K. Zvezdin, M. Bayer, Nat. Nanotechnol. 6 (2011) 370–376.
[8] X. Yin, Z. Ye, J. Rho, Y. Wang, X. Zhang, Science 339 (2013) 1405–1407.
[9] P.K. Jain, Y. Xiao, R. Walsworth, A.E. Cohen, Nano Lett. 9 (2009) 1644–1650.
[10] J.Y. Chin, T. Steinle, T. Wehlus, D. Dregely, T. Weiss, V.I. Belotelov, B. Stritzker, H. Giessen, Nat. Commun. 4 (2013) 1599.
[11] V.V. Temnov, G. Armelles, U. Woggon, D. Guzatov, A. Cebollada, A. Garcia-Martin, J.M. Garcia-Martin, T. Thomay, A. Leitenstorfer, R. Bratschitsch, Nat. Photon. 4 (2010) 107–111.
[12] V.I. Belotelov, I.A. Akimov, M. Pohl, V.A. Kotov, S. Kasture, A.S. Vengurlekar, A.V. Gopal, D.R. Yakovlev, A.K. Zvezdin, M. Bayer, Nat. Nanotechnol. 6 (2011) 370–376.
[13] A.M. Humphries, T. Wang, E.R.J. Edwards, S.R. Allen, J.M. Shaw, H.T. Nembach, J.Q. Xiao, T.J. Silva, X. Fan, Nat. Commun. 8 (2017) 911.
[14] M. Montazeri, P. Upadhyaya, M.C. Onbasli, G. Yu, K.L. Wong, M. Lang, Y. Fan, X. Li, P. KhaliliAmiri, R.N. Schwartz, C.A. Ross, K.L. Wang, Nat. Commun. 6 (2015) 8958.
[15] P. Hansen, K. Witter, W. Tolksdorf, Phys. Rev. B 27 (1983) 6608.
[16] A. Kehlberger, K. Richter, M.C. Onbasli, G. Jakob, D.H. Kim, T. Goto, C.A. Ross, G. Götz, G. Reiss, T. Kuschel, M. Kläui,Phys. Rev. Appl. 4 (2015), 014008.

[17] M.C. Onbasli, L. Beran, M. Zahradnik, M. Kucera, R. Antos, J. Mistrik, G.F. Dionne, M. Veis, C.A. Ross, Sci. Rep. 6 (2016) 23640.
[18] J. Qin, Y. Zhang, X. Liang, C. Liu, C. Wang, T. Kang, H. Lu, L. Zhang, P. Zhou, X. Wang, B. Peng, J. Hu, L. Deng, L. Bi, ACS Photonics 4 (2017) 1403–1412.
[19] H.B. Vasili, B. Casals, R. Cichelero, F. Macià, J. Geshev, P. Gargiani, M. Valvidares, J. Herrero-Martin, E. Pellegrin, J. Fontcuberta, G. Herranz,Phys. Rev. B 96 (2017), 014433.
[20] Y.M. Koroteev, G. Bihlmayer, J.E. Gayone, E.V. Chulkov, S. Blugel, P.M. Echenique, P. Hofmann,Phys. Rev. Lett. 93 (2004), 046403.
[21] S. Murakami,Phys. Rev. Lett. 97 (2006), 236805.
[22] R.W. Zhang, C.W. Zhang, W.X. Ji, S.S. Yan, Y.G. Yao, Nanoscale 9 (2017) 8207–8212.
[23] W.K. Tse, A.H. MacDonald,Phys. Rev. Lett. 105 (2010), 057401.
[24] J. Toudert, R. Serna, M.J. de Castro, J. Phys. Chem. C 116 (2012) 20530–20539.
[25] A. Layadi, W. Cain, J.W. Lee, J. Artman, IEEE Trans. Magn. 23 (1987) 2993–2995.
[26] H. Wang, C. Du, P.C. Hammel, F. Yang,Phys. Rev. B 89 (2014), 134404.
[27] A. Crépieux, C. Lacroix, J. Magn. Magn. Mater. 182 (1998) 341–349.
[28] K. Di, V.L. Zhang, H.S. Lim, S.C. Ng, M.H. Kuok, J. Yu, J. Yoon, X. Qiu, H. Yang,Phys. Rev. Lett. 114 (2015), 047201.
[29] R.A. Gallardo, D. Cortés-Ortuño, T. Schneider, A. Roldán-Molina, F. Ma, R.E. Troncoso, K. Lenz, H. Fangohr, J. Lindner, P. Landeros,Phys. Rev. Lett. 122 (2019), 067204.
[30] T. Matsumoto, Y.G. So, Y. Kohno, Y. Ikuhara, N. Shibata, Nano Lett. 18 (2018) 754–762.
[31] O. Boulle, J. Vogel, H. Yang, S. Pizzini, D. de Souza Chaves, A. Locatelli, T.O. Menteş, A. Sala, L.D. Buda-Prejbeanu, O. Klein, M. Belmeguenai, Y. Roussigné, A. Stashkevich, S.M. Chérif, L. Aballe, M. Foerster, M. Chshiev, S. Auffret, I.M. Miron, G. Gaudin, Nat. Nanotechnol. 11 (2016) 449–454.
[32] A. Takayama, T. Sato, S. Souma, T. Takahashi,Phys. Rev. Lett. 106 (2011), 166401.
[33] J.P. Hanke, F. Freimuth, C. Niu, S. Blügel, Y. Mokrousov, Nat. Commun. 8 (2017) 1479.
[34] C. Niu, G. Bihlmayer, H. Zhang, D. Wortmann, S. Blugel, Y. Mokrousov, Phys. Rev. B 91 (2015), 041303(R).
[35] S.S. Kalarickal, P. Krivosik, M.Z. Wu, C.E. Patton, M.L. Schneider, P. Kabos, T.J. Silva, J.P. Nibarger,J. Appl. Phys. 99 (2006), 093909.
[36] Y. Tserkovnyak, A. Brataas, G.E.W. Bauer, B.I. Halperin, Rev. Mod. Phys. 77 (2005) 1375–1421.
[37] Y. Sun, H. Chang, M. Kabatek, Y.Y. Song, Z. Wang, M. Jantz, W. Schneider, M. Wu, E. Montoya, B. Kardasz, B. Heinrich, S.G.T. Velthuis, H. Schultheiss, A. Hoffmann,Phys. Rev. Lett. 111 (2013), 106601.
[38] H.L. Wang, C.H. Du, Y. Pu, R. Adur, P.C. Hammel, F.Y. Yang,Phys. Rev. Lett. 112 (2014), 197201.
[39] P.B.A. Fechine, E.N. Silva, A.S.D. Menezes, J. Derov, J.W. Stewart, A.J. Drehman, I.F. Vasconcelos, A.P. Ayala, L.P. Cardoso, A.S.B. Sombra, J. Phys. Chem. Solids 70 (2009) 202–209.
[40] L. Fernandez-Garcia, M. Suarez, J.L. Menendez, J. Alloys Compd. 495 (2010) 196–199.
[41] D.V.M. Paiva, M.A.S. Silva, T.S. Ribeiro, I.F. Vasconcelos, A.S.B. Sombra, J.C. Góes, P.B.A. Fechine, J. Alloys Compd. 644 (2015) 763–769.
[42] V. Monteseguro, P. Rodríguez-Hernández, R. Vilaplana, F.J. Manjón, V. Venkatramu, D. Errandonea, V. Lavín, A. Muñoz, J. Phys. Chem. C 118 (2014) 13177–13185.
[43] J.T. Krug, G.D. Wang, S.R. Emory, S. Nie, J. Am. Chem. Soc. 121 (1999) 9208–9214.
[44] J. Zhang, X. Li, X. Sun, Y. Li, J. Phys. Chem. B 109 (2005) 12544–12548.
[45] H. Lu, H. Zhang, X. Yu, S. Zeng, K.T. Yong, H.P. Ho, Plasmonics 7 (2012) 167–173.
[46] J. Toudert, R. Serna, M.J. de Castro, J. Phys. Chem. C 116 (2012) 20530–20539.
[47] A.G. Bezerra, P. Cavassin, T.N. Machado, T.D. Woiski, R. Caetano, W.H. Schreiner, J. Nanopart. Res. 19 (2017) 362.
[48] T. Gaudisson, U. Acevedo, S. Nowak, N. Yaacoub, J.M. Greneche, S. Ammar, R. Valenzuela, J. Am. Ceram. Soc. 96 (2013) 3094–3099.
[49] P. Hofmann, Prog. Surf. Sci. 81 (2006) 191–245.
[50] F. Schindler, Z. Wang, M.G. Vergniory, A.M. Cook, A. Murani, S. Sengupta, A.Y. Kasumov, R. Deblock, S. Jeon, I. Drozdov, H. Bouchiat, S. Guéron, A. Yazdani, B.A. Bernevig, T. Neupert, Nat. Phys. 14 (2018) 918–924.
[51] H. Lu, S.D. Li, J. Mater. Chem. C 1 (2013) 3677–3680.
[52] J.F. Li, C.Y. Li, R.F. Aroca, Chem. Soc. Rev. 46 (2017) 3962–3979.
[53] P.F. Guo, S. Wu, Q.J. Ren, J. Lu, Z. Chen, S.J. Xiao, Y.Y. Zhu, J. Phys. Chem. Lett. 1 (2010) 315–318.
[54] F. Dong, T. Xiong, Y. Sun, Z. Zhao, Y. Zhou, X. Feng, Z. Wu, Chem. Commun. 50 (2014) 10386–10389.
[55] J. Toudert, R. Serna, I. Camps, J. Wojcik, P. Mascher, E. Rebollar, T.A. Ezquerra, J. Phys. Chem. C 121 (2017) 3511–3521.
[56] R. Tediosi, N.P. Armitage, E. Giannini, D. van der Marel,Phys. Rev. Lett. 99 (2007), 016406.
[57] V.B. Nascimento, V.E. de Carvalho, R. Paniago, E.A. Soares, L.O. Ladeira, H.D. Pfannes, J. Electron Spectrosc, Relat. Phenom. 104 (1999) 99–107.
[58] G. Armelles, A. Cebollada, A. García-Martín, M.U. González, Adv. Opt. Mater. 1 (2013) 10–35.
[59] K. Lodewijks, N. Maccaferri, T. Pakizeh, R.K. Dumas, I. Zubritskaya, J. Akerman, P. Vavassori, A. Dmitriev, Nano Lett. 14 (2014) 7207–7214.